

Synthesis and Physical Properties of Phase-Engineered Transition Metal Dichalcogenide Monolayer Heterostructures

Carl H. Naylor, William M. Parkin, Zhaoli Gao, Joel Berry, Songsong Zhou, qicheng zhang, John Brandon McClimon, Liang Z. Tan, christopher e kehayias, Meng-Qiang Zhao, ram s gona, Robert W Carpick, Andrew M. Rappe, David J Srolovitz, Marija Drndic, and Alan T. Charlie Johnson

ACS Nano, **Just Accepted Manuscript** • DOI: 10.1021/acsnano.7b03828 • Publication Date (Web): 02 Aug 2017

Downloaded from <http://pubs.acs.org> on August 11, 2017

Just Accepted

"Just Accepted" manuscripts have been peer-reviewed and accepted for publication. They are posted online prior to technical editing, formatting for publication and author proofing. The American Chemical Society provides "Just Accepted" as a free service to the research community to expedite the dissemination of scientific material as soon as possible after acceptance. "Just Accepted" manuscripts appear in full in PDF format accompanied by an HTML abstract. "Just Accepted" manuscripts have been fully peer reviewed, but should not be considered the official version of record. They are accessible to all readers and citable by the Digital Object Identifier (DOI®). "Just Accepted" is an optional service offered to authors. Therefore, the "Just Accepted" Web site may not include all articles that will be published in the journal. After a manuscript is technically edited and formatted, it will be removed from the "Just Accepted" Web site and published as an ASAP article. Note that technical editing may introduce minor changes to the manuscript text and/or graphics which could affect content, and all legal disclaimers and ethical guidelines that apply to the journal pertain. ACS cannot be held responsible for errors or consequences arising from the use of information contained in these "Just Accepted" manuscripts.



Synthesis and Physical Properties of Phase-Engineered Transition Metal Dichalcogenide Monolayer Heterostructures

Carl H. Naylor,¹ William M. Parkin,¹ Zhaoli Gao,¹ Joel Berry,² Songsong Zhou,² Qicheng Zhang,¹ John Brandon McClimon,² Liang Z. Tan,³ Christopher E. Kehayias,¹ Meng-Qiang Zhao,¹ Ram S. Gona,¹ Robert W. Carpick,^{2,4} Andrew M. Rappe,³ David J. Srolovitz,^{2,4} Marija Drndic,¹ Alan T. Charlie Johnson^{1}*

¹Department of Physics and Astronomy, University of Pennsylvania,

²Department of Materials Science and Engineering, University of Pennsylvania,

³Department of Chemistry, University of Pennsylvania,

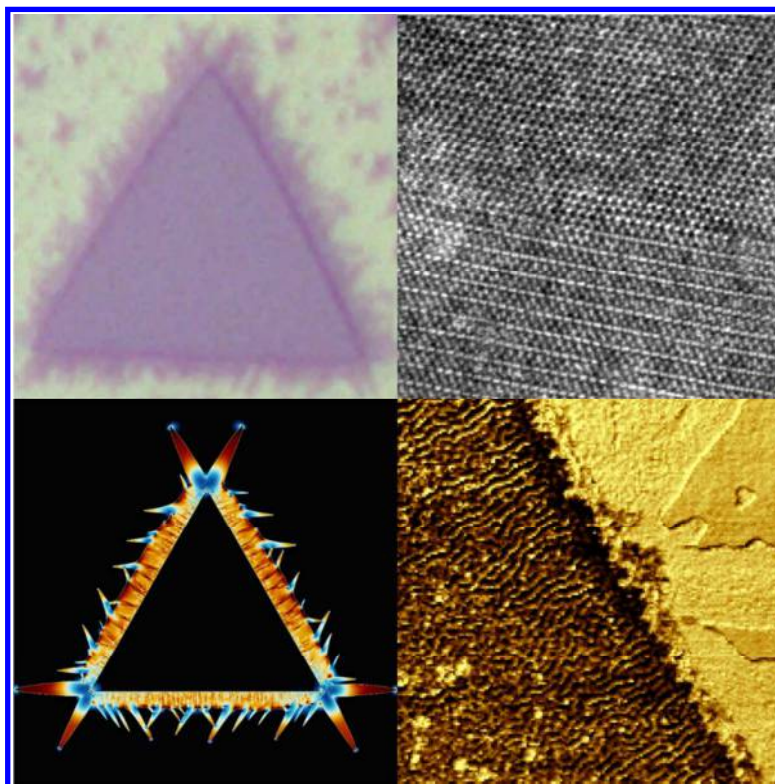
⁴Department of Mechanical Engineering and Applied Mechanics, University of Pennsylvania,

Philadelphia, Pennsylvania 19104, United States

KEYWORDS. heterostructure, phase-engineering, chemical vapor deposition, monolayer, two dimensional materials.

1
2
3 ABSTRACT. Heterostructures of transition metal dichalcogenides (TMDs) offer the attractive
4 prospect of combining distinct physical properties derived from different TMD structures. Here
5 we report direct chemical vapor deposition of in-plane monolayer heterostructures based on 1H-
6 MoS₂ and 1T'-MoTe₂. The large lattice mismatch between these materials led to intriguing
7 phenomena at their interface. Atomic force microscopy indicated buckling in the 1H region. Tip-
8 enhanced Raman spectroscopy showed mode structure consistent with Te substitution in the 1H
9 region during 1T'-MoTe₂ growth. This was confirmed by atomic resolution transmission electron
10 microscopy, which also revealed an atomically-stitched, dislocation-free 1H/1T' interface.
11 Theoretical modeling revealed that both the buckling and absence of interfacial misfit
12 dislocations were explained by lateral gradients in Te substitution levels within the 1H region
13 and elastic coupling between 1H and 1T' domains. Phase field simulations predicted 1T'
14 morphologies with spike-shaped islands at specific orientations consistent with experiments.
15 Electrical measurements across the heterostructure confirmed its electrical continuity. This work
16 demonstrates the feasibility of dislocation-free stitching of two different atomic configurations
17 and a pathway towards direct synthesis of monolayer TMD heterostructures of different phases.
18
19
20
21
22
23
24
25
26
27
28
29
30
31
32
33
34
35
36
37
38
39
40
41
42

43 TOC:
44
45
46
47
48
49
50
51
52
53
54
55
56
57
58
59
60



The study of two-dimensional materials “beyond graphene” has grown rapidly.^{1,2} Transition metal dichalcogenides (TMDs) are a broad materials family whose diverse composition and atomic structures enable numerous different physical and chemical properties.^{3–6} TMDs consist of sandwiches of metal (*e.g.* Mo, W) and chalcogen atoms (S, Se or Te) that in monolayer form assume atomic configurations known as the 1H, 1T and 1T’ phases (Figure 1a).^{7–11} In the 1H phase, the top and bottom chalcogen layers are aligned, while in the 1T phase, the layers are shifted relative to each other, forming a hexagon of chalcogen atoms when viewed normal to the plane. The 1T’ phase results from a distortion of the 1T structure resulting in an isolated chain of chalcogen atoms.

One method to produce monolayer TMDs is mechanical or liquid exfoliation of the bulk. Mechanical exfoliation relies on adhesive tape to peel apart a layered crystal to monolayer

1
2
3 thickness.¹² This yields high-quality monolayer material but very low surface coverage, making
4
5 the method tedious and not manufacturable. Liquid exfoliation relies on polymers and sonication
6
7 to dissociate bulk crystals. It yields many monolayer regions but also unwanted surface
8
9 contamination and/or structural damage.¹³ Monolayer TMD flakes can also be grown by
10
11 chemical vapor deposition (CVD) using solid or vapor precursors. The method is reproducible
12
13 and yields large amounts of high quality monolayer TMDs.^{14–17}
14
15
16

17
18 Of the TMDs, 1H-MoS₂ and 1H-WS₂ are the most widely synthesized and studied to date.^{18–22}
19
20 They are semiconductors with high on/off ratios, reasonable mobility values, large
21
22 photoluminescence, and energy band gaps whose size is tuned by the thickness of the flake.^{21,23}
23
24 Monolayer 1H-MoS₂ (a semiconductor) can be transformed into metallic 1T-MoS₂ through
25
26 chemical treatment with n-butyllithium, which was used to create a 1H-MoS₂/1T-MoS₂
27
28 heterostructure.¹¹ However 1T-MoS₂ is unstable in air, and n-butyllithium is pyrophoric,
29
30 complicating this approach. Groups have also reported phase transformations of exfoliated 1H-
31
32 MoS₂ by rhenium intercalation and thermal annealing,²⁴ and laser-enabled phase patterning of
33
34 few-layer exfoliated MoTe₂ to yield 1H/1T' heterostructures.⁹ To our knowledge, the synthesis
35
36 of in-plane heterostructures of monolayer TMDs of different atomic configuration has not been
37
38 reported to date.
39
40
41
42

43
44 1T'-MoTe₂ and 1T'-WTe₂ are semimetals that exhibit fascinating properties, including Weyl
45
46 semimetallicity,²⁵ superconductivity,²⁶ large non-saturating magnetoresistance,²⁷ quantum spin
47
48 hall effect,⁷ and weak antilocalization.^{16,28} These properties motivated efforts towards synthesis
49
50 of monolayer 1T' TMDs. We reported growth of high-quality monolayer 1T'-MoTe₂ and 1T'-
51
52 WTe₂, along with physical property measurement and analysis.^{16,28} These materials degrade
53
54 rapidly in air but can be stabilized to enable detailed property measurements. Others have also
55
56
57
58
59
60

reported synthesis of monolayer 1T' TMDs and observed optical dichroism and superconductivity.^{29,30} In-plane lateral heterostructures that combine TMDs in the 1H and 1T' structure are of significant interest because they offer the prospect of multifunctional capability that cannot be obtained from heterostructures based solely on the 1H phase.

Here we report synthesis of monolayer 1H-MoS₂/1T'-MoTe₂, atomically "stitched" heterostructures. We also developed a method to passivate the heterostructure flakes using large-area CVD graphene. X-ray Photoelectron Spectroscopy (XPS) confirmed the chemical composition of the sample. Tip enhanced Raman spectroscopy (TERS) demonstrated the distinction between the 1H and 1T' regions. The observed Raman modes were consistent with Density Functional Perturbation Theory (DFPT)³¹ calculations and suggested Te-for-S substitution in the 1H-MoS₂ region. Atomic force microscopy (AFM) showed that heterostructure flakes were monolayers with buckling in the 1H region. DFPT simulations revealed a buckling mechanism due to Te substitution in the 1H-MoS₂ and a growth mechanism that correlated with observations. Aberration corrected scanning transmission electron microscopy (ACSTEM) images confirmed the 1H and 1T' atomic configurations within a monolayer as well as the interfacial stitching structure. ACSTEM images also showed significant Te substitution in the 1H-MoS₂ region. Finally, we performed electrical measurements of a single 1H-1T' heterostructure flake and found that 1H-MoS₂ remained semiconducting in the presence of Te substitution and interfacial buckling. This study reveals a promising pathway to creation of in-plane TMD heterostructures and motivates further work towards combining relatively unexplored 1T' TMDs with 1H TMDs.

Results/Discussion

1
2
3 CVD synthesis of monolayer 1H/1T' was accomplished using ammonium
4 heptamolybdate (AHM) and vapors of sulfur and tellurium as precursors (Figure 1b; growth
5 details are provided in Methods). We first grew single-crystal 1H-MoS₂ flakes and then switched
6 furnace conditions for growth of 1T'-MoTe₂ single-crystal flakes, which nucleated at 1H-MoS₂
7 edges to form a stitched heterophase interface (Figure 1c). Figure 1d shows a “coffee ring” of
8 material around the AHM. At higher magnification (Figure 1d) triangular 1H flakes are seen
9 with 1T' needles growing from them, yielding a 1H/1T' heterostructure.
10
11
12
13
14
15
16
17
18
19
20
21
22
23
24
25
26
27
28
29
30
31
32
33
34
35
36
37
38
39
40
41
42
43
44
45
46
47
48
49
50
51
52
53
54
55
56
57
58
59
60

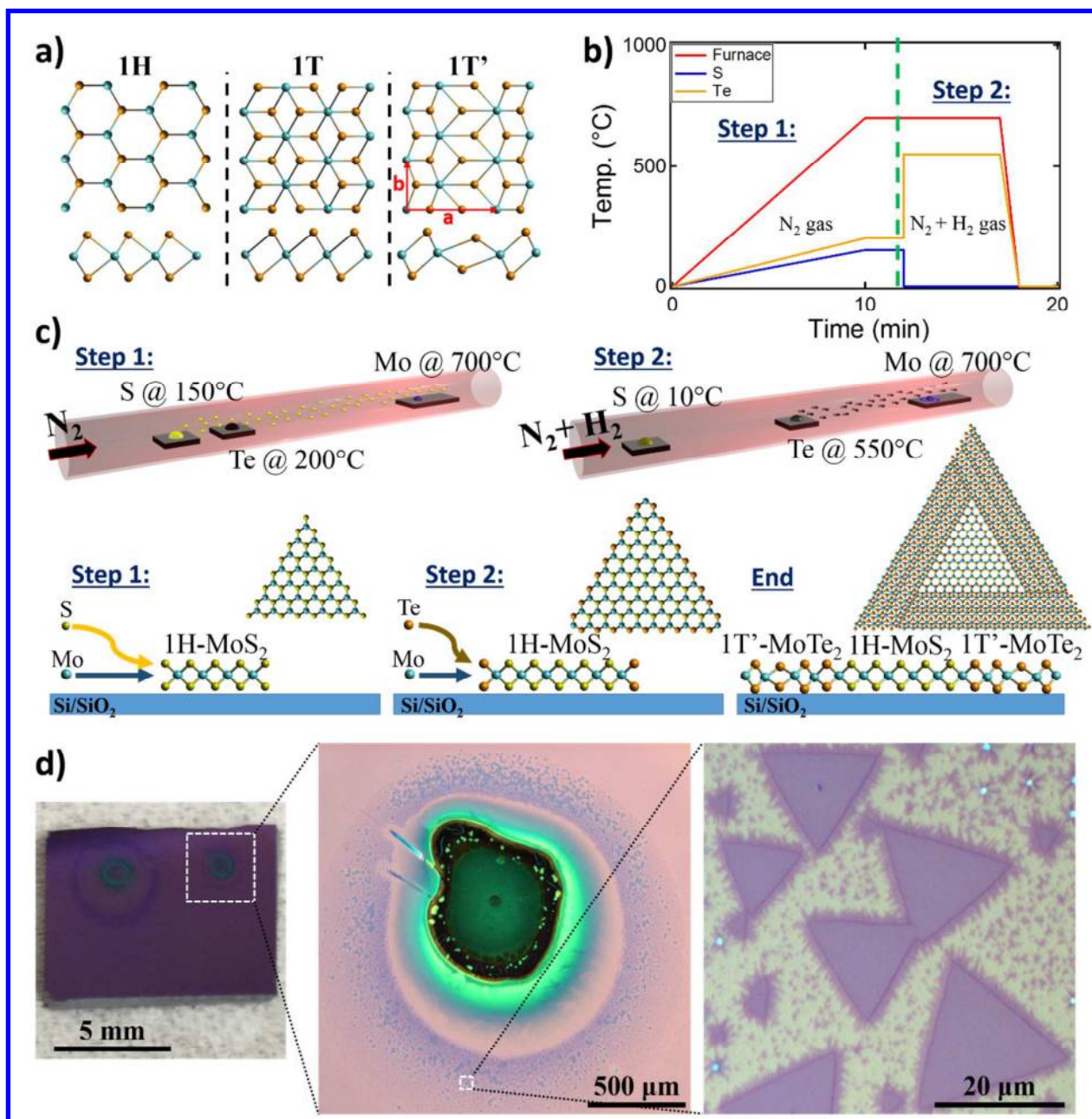


Figure 1. 1H/1T' growth. a) Ball and stick diagrams for the 1H, 1T, and 1T' phases of monolayer metal dichalcogenides (metal atom in blue and chalcogen in orange). b) Flow graph of the two-step growth process. c) Schematic of the growth setup and process. d) Optical micrographs of 1H/1T' flakes under increasing magnification.

1
2
3 XPS was performed on 1H/1T' heterostructures to confirm their composition (Figure 2a). We
4
5 identified the MoX_2 ($3d_{5/2}$, $3d_{3/2}$) peaks, as well as peaks for Te ($3d_{5/2}$, $3d_{3/2}$) and S ($2s$, $2p_{3/2}$,
6
7 $2p_{1/2}$), confirming the presence of Mo, S, and Te in the flakes. We also identified MoO_3 and
8
9 MoO_2 ($3d_{5/2}$, $3d_{3/2}$) peaks, which is ascribed to reaction of 1T'- MoTe_2 with ambient O_2 .^{16,28,32,33}
10
11
12
13
14
15
16
17
18
19
20
21
22
23
24
25
26
27
28
29
30
31
32
33
34
35
36
37
38
39
40
41
42
43
44
45
46
47
48
49
50
51
52
53
54
55
56
57
58
59
60

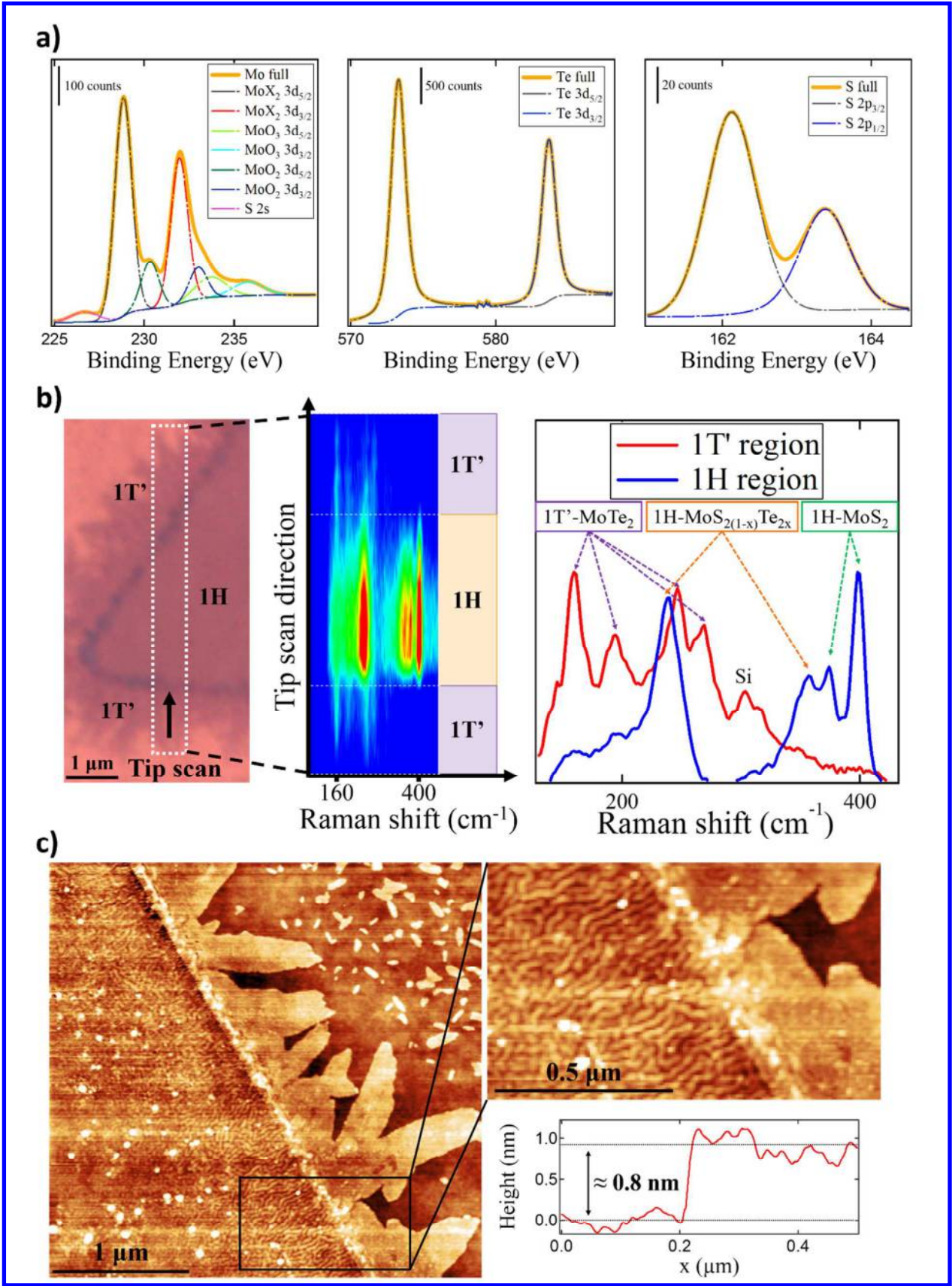


Figure 2. Characterization of 1H/1T' heterostructure flakes. a) X-ray photoelectron spectroscopy (XPS) data revealing the presence Mo, S and Te compounds in the flake. b) Tip-enhanced Raman spectroscopy results show clear differences between the 1H and 1T' regions. c) AFM of a 1H/1T' flake indicates monolayer height and the presence of wrinkles indicative of buckling of the 1H region.

Tip-enhanced Raman spectroscopy (TERS) was used to study the vibrational spectrum of different regions of the heterostructure. Since 1T'-MoTe₂ decays rapidly in air, the heterostructure growth substrate was covered with CVD-grown graphene before conducting measurements. For the data in Figure 2b, the scan line begins in a 1T' region, moves through 1H material and then concludes in a 1T' section. The three regions were differentiated in the TERS map (Figure 2b) and their Raman-active modes were identified. In the 1T' regions (beginning and end of the scan line), we identified five modes at 160 cm⁻¹, 190 cm⁻¹, 248 cm⁻¹, 269 cm⁻¹, and 300 cm⁻¹; the last is due to the Si substrate.³⁴ The other four peaks are the A_g modes of monolayer 1T'-MoTe₂, and the values are in excellent agreement with previous reports and theoretical predictions.^{16,32,35} The 269 cm⁻¹ peak is confirmation of 1T'-MoTe₂ in monolayer form, because this spectral line shifts for multi-layer material, towards a value of 258 cm⁻¹ for the bulk.³⁶

In the center of the flake (1H region), we identified four modes: 240 cm⁻¹, 359 cm⁻¹, 372 cm⁻¹ and 400 cm⁻¹. Stoichiometric 1H-MoS₂ exhibits two peaks, E_{2g}¹ and A_{1g}. We performed DFPT calculations of 1H-MoS₂ and found modes at 376 cm⁻¹ and 395 cm⁻¹, consistent with previous reports.^{20,37} These modes occur at frequencies similar to those observed at 372 cm⁻¹ and 400 cm⁻¹, suggesting the presence of 1H-MoS₂ in the 1H region of the heterostructure. To explain the

other two modes seen in TERS (240 cm^{-1} and 359 cm^{-1}), we performed DFPT simulations on $1\text{H-MoS}_{2(1-x)}\text{Te}_{2x}$ for $x = 0.25$ and $x = 0.5$. The E_{2g}^1 and A_{1g} modes both redshift due to the more massive Te atoms. The E_{2g} mode redshifts from 376 cm^{-1} to 349 cm^{-1} (340 cm^{-1}) for $x = 0.25$ ($x = 0.5$) while the A_{1g} mode shifts dramatically from 395 cm^{-1} to 243 cm^{-1} (217 cm^{-1}). These two modes characteristic of $1\text{H-MoS}_{2(1-x)}\text{Te}_{2x}$ closely match the 359 cm^{-1} and 240 cm^{-1} modes observed for the 1H region in the heterostructure, with better agreement for $x \sim 0.25$; moreover the intensity of the A_{1g} 400 cm^{-1} mode is close to the 240 cm^{-1} and the E_{2g} 372 cm^{-1} matches the 359 cm^{-1} , consistent with this assignment. We therefore propose a model for heterostructure growth, where the triangular region was first grown as 1H-MoS₂ but then during growth of the 1T'-MoTe₂ region, Te atoms insert into some S sites, converting nanoscale regions of the triangle into 1H-MoS₂/1H-Mo MoS_{2(1-x)}Te_{2x} with $0.25 \leq x \leq 0.5$. These TERS results confirm the 1H/1T' nature of the heterostructure flakes and the identity of the 1T'-MoTe₂ material, and they also suggest the existence of Te substitution for S in the triangular 1H-MoS₂ region. This latter finding is consistent with DFT-based calculations³⁸ which indicate that 1H-MoS_{2(1-x)}Te_{2x} alloy thermodynamics favors mixing S and Te into a solid solution for $T \geq 230^\circ\text{C}$, while phase separation into Te-rich and S-rich domains is preferred for $T \leq 230^\circ\text{C}$.

Atomic force microscopy (AFM) was used to investigate the height and structure of the heterostructure flakes (Figure 2c). We measured a height of approximately 0.8 nm at the edge of the flake, consistent with monolayer material, and noticed small multilayer regions along portions of the 1H/1T' interface. This indicates that 1T'-MoTe₂ growth occurred at the 1H-MoS₂ edge, preferentially in-plane but with some out-of-plane growth. We observed wrinkles at the 1H/1T' interface that extend $\sim 500\text{ nm}$ into the 1H region. The observation of buckled 1H regions and flat 1T' regions is surprising considering the misfit between 1H-MoS₂ and 1T'-MoTe₂

crystals. In equilibrium $b_{1H-MoS_2} = 3.183 \text{ \AA}$ and $b_{1T'-MoTe_2} = 3.455 \text{ \AA}$,¹⁰ such that the 1H side is under $\epsilon_0^{1H} \simeq 8.5\%$ (tensile) strain and the 1T' side is under $\epsilon_0^{1T'} \simeq -7.9\%$ (compressive) strain. If buckling occurs, it is expected in the 1T' region, not as observed in the 1H region. We return to this below.

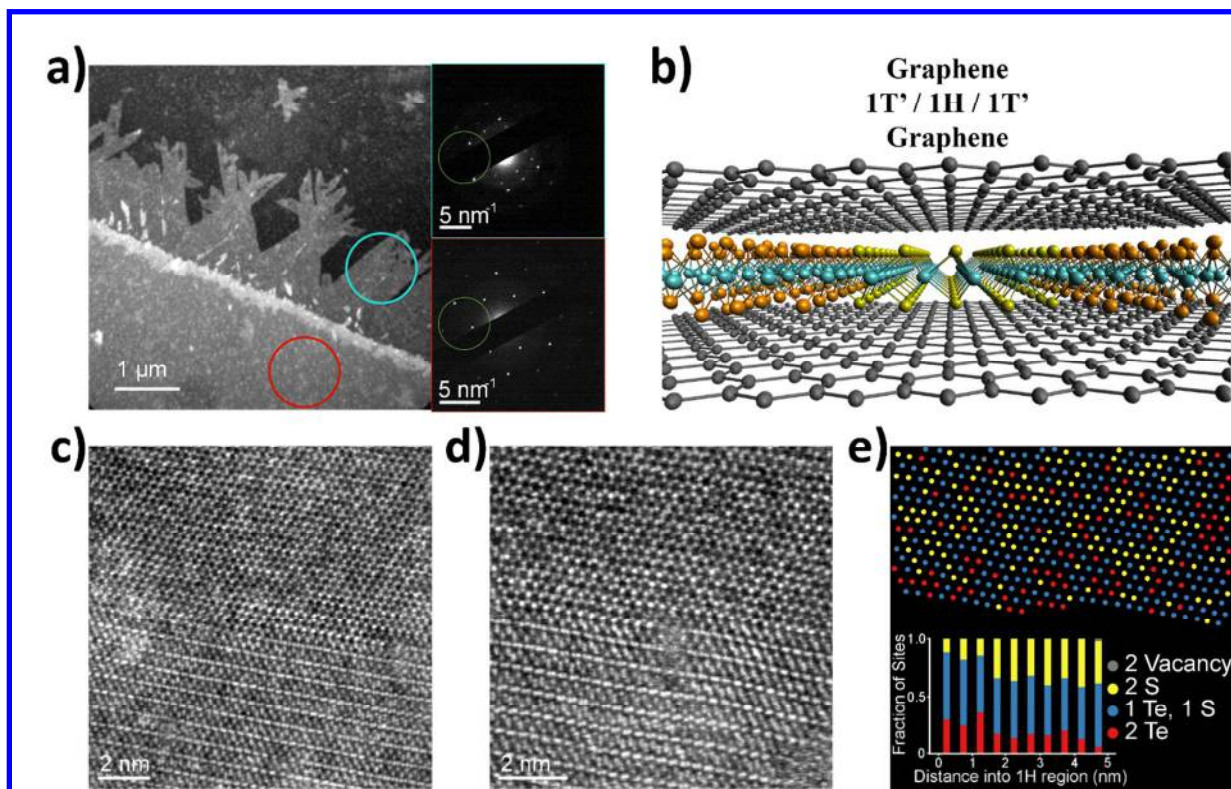


Figure 3. Characterization by Transmission Electron Microscopy (TEM). a) Dark-field TEM micrograph of the interface between a 1H region (bottom) and 1T' region (top) of a flake on a TEM carbon grid. The top-right image shows selected area electron diffraction (SAED) pattern from the circled 1T' region, and the bottom-right image shows a SAED pattern from the circled 1H region. A large objective aperture was used to select several diffracted beams (approximate aperture in green). b) Schematic of graphene encapsulating a 1H/1T' heterostructure used for ACSTEM measurements. c,d) Aberration-corrected high angle annular dark field (HAADF)

images of the interface between 1H and 1T'. e) Sulfur sites in the MoS₂ region in d) labeled with number of tellurium substitutions estimated using the intensity of the site in the HAADF image. Inset is the occurrence of each substitution type as a function of distance from the boundary.

Selected area electron diffraction (SAED) on regions of a heterostructure flake (Figure 3a) showed that the 1T'-MoTe₂ flakes grew fastest along the Te zigzag chain direction, resulting in a rectangular morphology with the long axis along the [010] crystal direction, consistent with our earlier report.¹⁶ SAED also showed that the edges of the 1H region were oriented along its zigzag direction and that the [010] directions in the 1T'-MoTe₂ flakes were oriented at 60° and 120° from parallel to the interface.

In order to gain understanding of the structure at the 1H-1T' interface, atomic resolution ACSTEM was conducted on heterostructure flakes that had been encapsulated between graphene sheets (Figure 3b; fabrication details are in Methods) to prevent oxidation.²⁸ Aberration corrected high angle annular dark field ACSTEM (HAADF) images showed that the orientation of rectangular 1T'-MoTe₂ regions away from the heterostructure interface did not directly reflect atomic stitching at the interface. Atomic resolution images (Figure 3c-d) of the 1H-1T' interface show that the stitching mainly consisted of 1H-MoS₂ zigzag edges stitched to 1T'-MoTe₂ zigzag edges. This edge stitching is not represented in the lower magnification image (Figure 3a) that shows 1T'-MoTe₂ flakes oriented 60° and 120° from the zigzag direction (see Fig. S1 for details).

It seems surprising that despite the large misfit strain between 1H-MoS₂ and 1T'-MoTe₂ (in MoTe₂ the strain is $\epsilon_0^{1T'} \simeq -7.9\%$), neither interfacial misfit dislocations nor buckling was observed in the 1T' phase (1H buckling is seen). To relieve the entire misfit would require a

large dislocation density with spacing $s_0 = |\mathbf{b}|/\varepsilon_0^{1T} \simeq 4$ nm (\mathbf{b} is the Burgers vector). We return to this below.

HAADF images also showed Te substitution near the interface. Since HAADF images are based upon mass contrast (intensity proportional to atomic number squared; $Z_S = 16$, $Z_{Mo} = 42$, $Z_{Te} = 52$), identifying Te substitutions is straightforward. Figure 3e shows S_2 sites in a 1H region near the interface labeled with the number of Te substitutions, based on the HAADF intensity (see Figure S2). Heterostructure growth introduced single and double Te substitutions in the 1H region, especially near the interface, in agreement with TERS measurements. Te levels near the 1H/1T' interface ($0.5 \lesssim x_i^{1H} \lesssim 0.75$, see Figure 3) are enhanced relative to those in the 1H triangle interior ($0.25 \lesssim x_0^{1H} \lesssim 0.5$ on average, see Figure 2).

This gradient in Te concentration between the 1H domain interior and the 1H side of the 1H/1T' interface generates the unexpected buckling on the 1H side. Te substitution creates biaxial compressive strain; the 1H lattice parameter increases with x_0^{1H} as $b_{1H}(x_0^{1H}) \simeq 3.183 + (3.55 - 3.183)x_0^{1H}$ (in Å). The compressive strain induced by Te substitution ($\varepsilon_{Te} \simeq 0.115x_0^{1H}$) therefore increases from the interior of the 1H triangle toward the 1H/1T' interface by between ~0% and ~5.5% (corresponding to $x_i^{1H} = x_0^{1H} = 0.5$ and $x_0^{1H} = 0.25$, $x_i^{1H} = 0.75$, respectively). This variation occurs over ~1 μm (see Figure 2b), which is consistent with the experimentally observed width of the buckled strip in the 1H phase ~0.5 μm (see Figure 2c).

The compressive strain associated with the Te concentration gradient can also be compared to the strain relieved by buckling. Using the wrinkle amplitude and wavelength from AFM images in Figure 2c ($A \simeq 0.4$ nm, $\lambda \simeq 25$ nm), we find that the strain relieved by buckling (in a one-dimensional sinusoidal approximation) is $\varepsilon_b = (L - L_0)/L_0 \simeq (\pi A/\lambda)^2 \simeq 0.25\%$, where L is the arc length of the 1D profile over a distance L_0 . This estimate of the strain released by the buckling

(of the observed wavelength and amplitude) is consistent with the strain produced by the gradient in the Te concentration (*i.e.*, $0 \leq \varepsilon \leq -5.5\%$).

The large Te fraction near the 1H/1T' interface also accounts for the absence of buckling in the 1T' domains and the observed lack of interfacial misfit dislocations. Figures 4a,b show the misfit strain on either side of the interface as a function of the concentrations on both sides of the interface, 1H-MoS_{2(1-x_i^{1H})Te_{2x_i^{1H}} and 1T'-MoS_{2(1-x_i^{1T'})Te_{2x_i^{1T'}}. We estimate $0.51 \leq x_i^{1H} \leq 0.75$ and $0.69 \leq x_i^{1T'} \leq 0.94$ from the lattice parameters in the ACSTEM images. This composition variation creates misfit strains $-2.6\% \leq \varepsilon_0^{1H} \leq 2.1\%$ and $-2.1\% \leq \varepsilon_0^{1T'} \leq 2.6\%$ (gray rectangles in Figures 4a-b). This demonstrates that even though 1T'-MoTe₂ would be expected to be in compression when bonded to 1H-MoS₂, the actual composition of these two phases makes the opposite possible (compression in the 1H phase, tension in 1T' – consistent with the observation of 1H buckling). Since the compressive strain in the 1H phase is released by buckling, no interfacial misfit dislocations need to form to relax the strain.}}

The buckling in the 1H phase appears to be one dimensional (1D) near the 1H/1T' interface and 2D further into the 1H. This indicates that the compressive stress near and tangential to the interface in 1H is larger than that perpendicular to it. This is consistent with the presence of tensile stresses in 1T' near the interface.

These findings demonstrate that thermodynamically-driven intermixing of chalcogen species qualitatively alters the interfacial properties and strains in MoS₂/MoTe₂ heterostructures from those that would be exhibited in the absence of compositional mixing. This highlights the fundamental roles of alloy thermodynamics, 2D material mechanics, and their inter-connection in determining the properties of 2D material heterostructures.

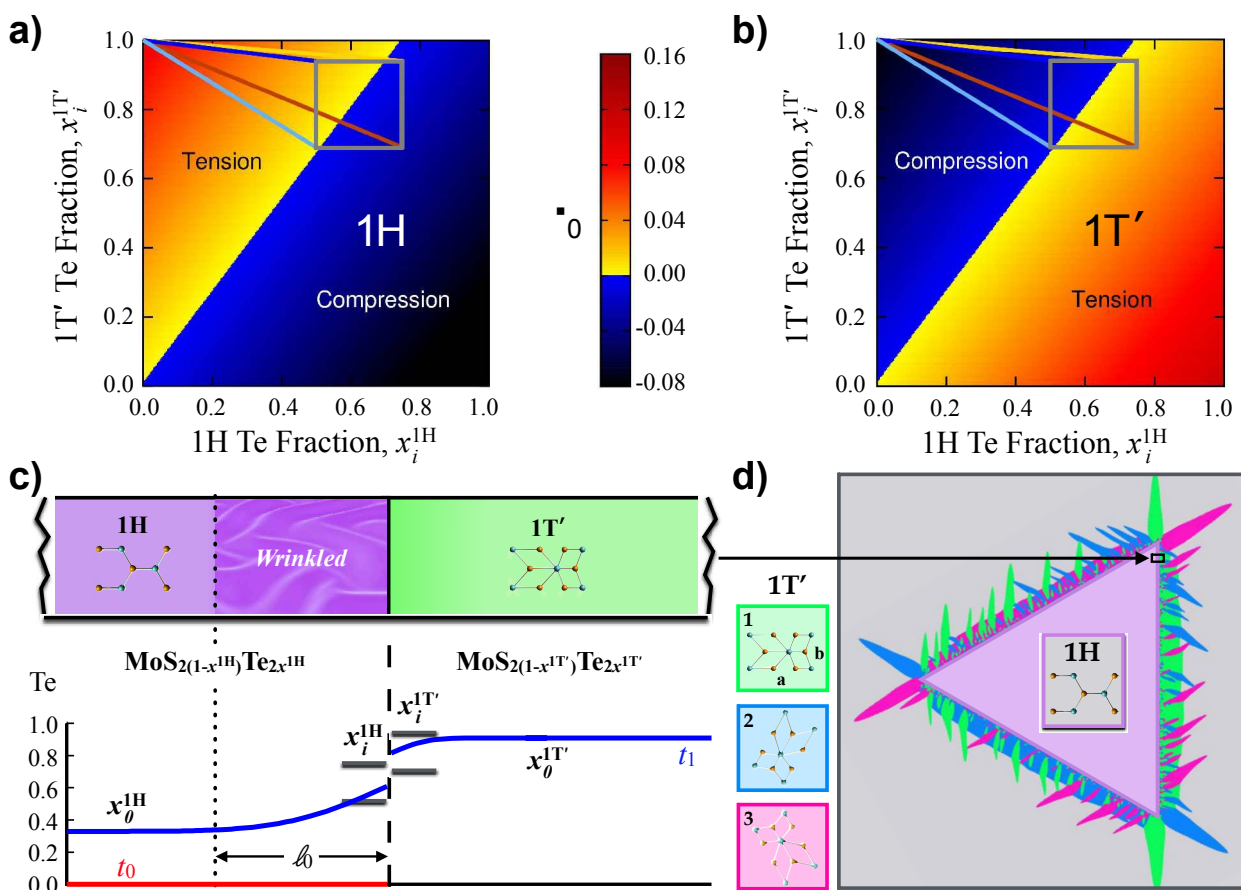


Figure 4. Effects of composition, elastic misfit strain, and out-of-plane bending on heterostructure interfaces and growth morphology. a) and b) are maps of misfit strain as a function of Te fractions x_i^{1H} and $x_i^{1T'}$ on the 1H and 1T' sides of the 1H/1T' interface, respectively. The gray rectangle encloses compositional bounds inferred from ACSTEM-derived lattice parameters near the interface. c) Schematic of compositional domains and variation of Te composition near the 1H/1T' interface. Configurations are shown at the end of 1H-MoS₂ growth (t_0 , red line) and at the end of 1T'-MoTe₂ growth (t_1 , blue lines). Gray shaded areas are bounds shown in a) and b). d) Simulated 1T' morphology at the misfit strain corresponding to $x_i^{1H} = 0.75$ and $x_i^{1T'} = 0.94$. The color scheme employed for T' domains is shown on the left.

The needle-like growth morphology of the 1T' domains differs from compact growth morphologies observed in lateral 1H/1H TMD heterostructures such as MoS₂/WS₂^{41,42} and MoSe₂/WSe₂.⁴³ In these systems the 1H crystals have nearly identical lattice parameters, so the second phase grows with little deviation from the morphology of the parent phase. In contrast, isolated single crystal 1T'-MoTe₂ flakes grow with needle-like shapes, with the short (*b*) direction aligned with the long edge of the flake.^{16,32} We performed DFT calculations which show that the *b* edge in 1T'-MoTe₂ has lower energy than the *a* edge ($\lesssim 200$ meV/Å and ~ 270 meV/Å, respectively), which leads to elongated equilibrium flake shapes that are consistent with experimental observations (see the Supporting Information and Figs. S3 – S4). Since 1T' nucleation occurs at the edge of the 1H flake, interface coherence dictates three possible orientations for the 1T' needles (*b* parallel to the flake edge or at 60° or 120°, see Figure 4d), precisely as observed in dark-field TEM images (Figure 3). An additional constraint in heterostructure growth, elastic coupling between phases, can independently control growth morphology. We performed continuum elastic phase field simulations of nucleation and growth of 1T' domains bound to an elastically misfitting parent 1H crystal. The model describes how 1T' domains form and evolve to minimize elastic misfit energy during displacive 1H → 1T' structural transformations⁴⁰ (see the Supporting Information and Figs. S5 – S6 for more details).

Figure 4d shows a representative morphology from a simulation with isotropic 1T' edge energies and misfit strain equal to that when $x_i^{1H} = 0.75$ and $x_i^{1T'} = 0.94$ (see Figure 4). The morphology is very similar to that of the synthesized heterostructure, with needles composed of two 1T' orientations at 60° or 120° from parallel to each triangular flake edge. A strip composed predominantly of the third orientation (0°) is observed along the inner portion of each edge, consistent with the observed [010] alignment of the 1H and 1T' lattices across the interface. A

relatively uniform, compact triangular growth morphology is obtained in the absence of elastic misfit or when the misfit strain is shear-dominant rather than dilatation-dominant (see the Supporting Information). These results demonstrate that elastic misfit alone can induce needle-like $1T'$ growth morphologies, even in the absence of anisotropic edge energies and growth rates. At the estimated misfit strain and computed edge anisotropy of the present system, we expect that both effects contribute to the observed needle-like morphologies.

Field effect transistor (FET) devices were made from single heterostructures (Figure 5a), after reshaping the flake. Fabrication details are provided in the Methods section. The device was inserted in a vacuum probe station, and electrical data collected at 10^{-7} Torr. Useful data were collected from five of 15 separate devices on one growth substrate, with very similar results. Care was taken to ensure there were no gate leaks and that measured responses were due to the monolayer device structure.

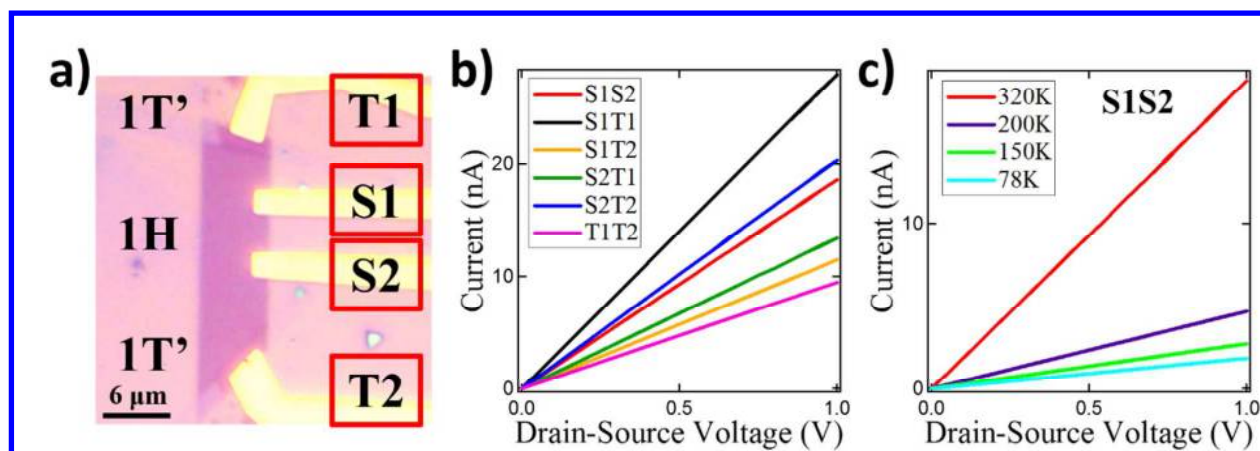


Figure 5. Electrical responses from the $1T'/1H/1T'$ structure. a) Optical micrograph of a $1T'/1H/1T'$ device taken after completion of the measurements. Lack of optical contrast for $1T'$ - $MoTe_2$ regions away from the contact are due to oxidation. b) Current-bias voltage (I-V)

characteristics for different contact pairs, measured at room temperature. c) I-V characteristic at different temperatures for the 1H-MoS₂ region (S1-S2 contact pair).

Figure 5b shows electrical responses through all possible connections and shows that the 1H/1T' interface is electrically continuous. Higher current was observed in all samples for the S1T1 and S2T2 contacts compared to the S1S2 pair, even though the S1S2 contact pair has the least separation, which is ascribed to reduced contact resistance due to the semi-metallic nature of the 1T' region. Figure 5c shows electrical transport through the 1H region at various temperatures. The current decreases with decreasing temperature, indicating that the 1H region remains semiconducting even with the buckling and Te substitution.

Conclusions

We developed a CVD synthesis of 1H/1T' monolayer TMD heterostructures. The chemical composition and atomic structure of the heterostructure flakes were confirmed by XPS, tip-enhanced Raman spectroscopy, AFM, and ACSTEM, with interpretation guided by DFPT simulations. The data show enhanced Te substitution in the 1H-MoS₂ region that is enhanced near the interface, leading to buckling. The growth resulted in three distinct 1T'-MoTe₂ variants that were atomically stitched to the 1H phase with no misfit dislocations, as confirmed through ACSTEM images. The overall morphology was replicated in continuum phase field elastic growth simulations. Electrical measurements confirmed that the 1H region maintained its semiconducting properties. Future work will be directed towards reducing the Te substitution in order to maintain the intrinsic 1H-MoS₂ properties. This work provides a pathway to in-depth

investigations of 1H/1T' TMD heterostructures and effects occurring at the one-dimensional interface of monolayer semiconductors and topological insulators.

Methods/Experimental

CVD synthesis of 1H/1T' heterostructures. The Si/SiO₂ growth substrate was prepared by spin coating a growth promoter of 1% sodium cholate at 3000 rpm for 60 seconds. Sodium cholate is known to act as a growth promoter for 1H-MoS₂ and 1T'-MoTe₂.^{14,16,44} A micro-droplet of a saturated solution of ammonium heptamolybdate (AHM) was deposited onto the substrate to provide the molybdenum feedstock. The chip was then inserted into the center of a CVD furnace, with two source chips placed upstream, one chip with 25 mg of sulfur and the second with 25mg of tellurium. The sulfur (tellurium) source was placed 18 cm (15 cm) from the growth substrate. The CVD furnace was then heated to 700°C at a rate of 70°C/min under a constant flow of 1000 sccm N₂. The S chip reached a temperature of 150°C and started to sublime, while the Te pellet was at 200°C, well below its sublimation temperature of 550°C (Figure 1c, step1). After 12 minutes of 1H-MoS₂ growth we used a magnetic system to slide the Te substrate closer to the growth substrate, where it rose in temperature to 550°C and began to sublime. We used the same system to slide the sulfur substrate away so that it rapidly cooled, and we adjusted the gas flow to 25 sccm H₂ and 400 sccm of N₂ (Figure 1c, step2). After a 5 minute growth time, the furnace was rapidly cooled and the substrate retrieved.

XPS. The sample was transferred directly from the growth chamber to the XPS system loadlock and pumped down within 20 min of growth to minimize sample oxidation. Measurements were performed in the constant analyzer energy mode using a customized XPS

spectrometer with a monochromatized Al K α source.⁴⁵ Data was analyzed using CasaXPS software (v2.3.16, Casa Software Ltd., Wilmslow, Cheshire, U.K.). The XPS spectrometer was calibrated in accordance with ISO 15472:2001 to an accuracy of better than ± 0.05 eV for the 100 eV pass energy used for the high resolution spectra and the 200 eV pass energy used for the survey spectra. High resolution spectra were fit with peak shapes composed of a convolution of Gaussian and Lorentzian functions superimposed atop a Shirley-Sherwood background.⁴⁶ Synthetic peaks were constrained to have appropriate intensity ratios for spin-orbit split states and the same FWHM, with the exception of the Mo 3d components for MoO₃. High resolution spectra revealed the presence of charging due to the thickness of the SiO_x layer on the Si substrate. This effect was corrected for all high resolution spectra by shifting the aliphatic carbon peak, which was the most intense component of the C1s spectra, to 285.0 eV.⁴⁷ Peak positions are reported as an average of the two analyzed regions along with the spread of the data. Mo 3d high resolution spectra were fit with seven components: S 2s at 226.65 ± 0.02 eV, Mo 3d^{5/2} from Te_xMo_yS_z at 228.85 ± 0.02 eV, MoO₂ 3d^{5/2} at 230.31 ± 0.01 eV, Te_xMo_yS_z 3d^{3/2} at 231.98 ± 0.03 eV, MoO₂ 3d^{3/2} at 233.04 ± 0.04 eV, MoO₃ 3d^{5/2} at 233.74 ± 0.04 eV, and MoO₃ 3d^{3/2} at 235.92 ± 0.16 eV.^{48,49} Te 3d spectra were fit with two components: Te 3d^{5/2} from Te_xMo_yS_z at 573.26 ± 0.01 eV and Te_xMo_yS_z 3d^{3/2} at 583.65 ± 0.02 eV. S 2p spectra were fit with two components: 2p^{3/2} from Te_xMo_yS_z at 162.15 ± 0.03 eV, and Te_xMo_yS_z 2p^{1/2} at 163.36 ± 0.02 eV.

Selected Area Electron Diffraction (SAED). The SAED patterns were taken in a JEOL 2100 operated at 200 kV. The heterostructure flakes were transferred onto a TEM carbon grid using a previously described HF transfer process.¹⁶ A selected-area aperture with a 1 μ m effective diameter at the specimen was used.

Graphene growth. Graphene synthesis was carried out in a low-pressure CVD furnace (OTF-1200X-4-C4-SL-UL, MTI Corp.). Cu foils (Alfa Aesar Item #46365) were cleaned with 5.4% HNO₃ for 40 seconds and two DI water baths for 2 min, and then blown dry with N₂ gas. The reaction chamber was pumped to a base pressure of ~ 50 mTorr. The Cu growth substrate was annealed at 1020 °C for 30 minutes under a gas flow of 500 sccm Ar and 80 sccm H₂. Monolayer graphene was then grown using methane as a carbon source at a flow rate of 5 sccm for 5 mins and then 10 sccm for 15 mins. The reactor was subsequently cooled to room temperature rapidly under a flow of 80 sccm H₂ and 10 sccm CH₄.

Graphene passivation. Monolayer graphene was grown by CVD following the recipe discussed in the previous paragraph. Two pieces of graphene on Cu foil were spin coated at 3000 rpm for 60 seconds with C4 PMMA and then released from the Cu foil by the bubble transfer method and left floating in deionized (DI) water. The first sheet of graphene was transferred onto the as-grown heterostructure flakes, and the second sheet of graphene was transferred onto a holey-carbon TEM grid. The PMMA layer on top of the graphene/TEM grid was dissolved with acetone, followed by isopropanol (IPA). The PMMA/graphene/1H-1T' heterostructure stack on the SiO₂/Si growth substrate was then released using a diluted HF solution of 1:25 and quickly washed in 2 DI water baths before being transferred onto the first graphene sheet on the TEM grid. Acetone was then used to dissolve the PMMA followed by IPA. We were then left with a graphene/1H-1T' heterostructure/graphene on a TEM grid (figure 3(b)). The sample was stable in this configuration and could be transported to the ACSTEM for high resolution imaging.

Aberration corrected HAADF. Aberration corrected HAADF imaging was performed with a JEOL ARM 200CF with a corrector on the STEM probe and operated at 80 kV. The flakes were encapsulated between two graphene layers and transferred onto a holey carbon grid to slow

oxidation outside of the TEM¹⁶ and electron-beam induced damage in the TEM, as the graphene is effectively invisible on MoS₂/MoTe₂ in the mass contrast HAADF images (Figure 3b).⁵⁰

Device fabrication. An as-grown sample of triangular 1H/1T' flakes was spin coated at 3000 rpm for 60 seconds with C4 PMMA. Electron beam lithography (EBL) and plasma etching were used to define a rectangular region where the ends of the rectangle were 1T' material while the center region was 1H. A new layer of C4 resist was then applied to the substrate and marker regions were patterned by EBL. Optical microscopy was used to locate the rectangular flake with respect to the markers. A final round of EBL was performed to pattern contacts that were aligned to the 1H and 1T' regions, and the contacts were metallized with 3nm of Cr and 40 nm of Au deposited by thermal evaporation. This was followed by lift-off in an acetone bath and a rinse in IPA. The sample was then dried by N₂ gun and immediately stored under vacuum for transfer to the measurement system.

ASSOCIATED CONTENT

Supporting Information.

The following files are available free of charge. Supporting information for simulations.

AUTHOR INFORMATION

Corresponding Author

*cjohnson@physics.upenn.edu.

Author Contributions

1
2
3 A.T.C.J. directed the research. C.H.N. proposed and designed the experiment, and carried out
4 1H-1T' growth and AFM measurements. J.B.M. performed XPS measurement under the
5 supervision of R.W.C. Q.Z., C.H.N and C.E.K. performed TERS measurements and analysis.
6
7 L.Z.T. performed Raman simulations under the supervision of A.M.R. W.M.P. performed TEM
8 measurements under the supervision of M.D. Graphene growth was carried out by Z.G. Device
9 fabrication and measurements were performed by C.H.N and R.S.G. The phase field simulations
10 and first principles calculations were performed by J.B. and S.Z. under the supervision of D.J.S.
11
12 C.H.N. and A.T.C.J. wrote the manuscript with input and approval from all authors.
13
14
15
16
17
18
19
20
21
22

23 **Funding Sources**

24
25 This work was supported by NSF EFRI 2-DARE 1542879 with additional support from NSF
26 MRSEC DMR-1120901. W.M.P. and M.D. acknowledge funding from NSF EFRI 2-DARE
27 (EFRI-1542707). The authors acknowledge use of the Raman mapping system supported by NSF
28 Major Research Instrumentation Grant DMR-0923245. The phase field simulations and first
29 principles calculations were supported as part of the Center for the Computational Design of
30 Functional Layered Materials, an Energy Frontier Research Center funded by the U.S.
31 Department of Energy (DOE), Office of Science, Basic Energy Sciences (BES) under Award
32 DE-SC0012575. L.Z.T. and A.M.R. acknowledge support from the US DOE through grant no.
33 DE-FG02-07ER15920. Computational support was provided by HPCMO of US DoD and
34 NERSC. J.B.M. and R.W.C. acknowledge support from NSF grant CMMI-133424.
35
36
37
38
39
40
41
42
43
44
45
46
47
48
49
50
51
52
53

54 **ACKNOWLEDGMENT**

55
56
57
58
59
60

The authors gratefully acknowledge use of the HR-TEM in the Krishna Singh Center for Nanotechnology at the University of Pennsylvania, the use of the AC-TEM facility at Lehigh University and useful discussions with Simeon Ristić.

Supporting Information

SAED and ACSTEM determination of lattice orientation. Histogram of intensities of S and Mo sites in Figure 3e. Characterization of 1H/1T' heterostructures. First principles calculations of 1T'-MoTe2 edge energies. Phase field simulations of heterostructure growth. This material is available free of charge via the Internet at <http://pubs.acs.org>.

REFERENCES

1. Geim, A. K. & Grigorieva, I. V. Van der Waals Heterostructures. *Nature* **2013**, 499, 419.

2. Bhimanapati, G. R.; Lin, Z.; Meunier, V.; Jung, Y.; Cha, J.; Das, S.; Xiao, D.; Son, Y.; Strano, M. S.; Cooper, V. R.; Liang, L.; Louie, S. G.; Ringe, E.; Zhou, W.; Kim, S. S.; Naik, R. R.; Sumpter, B. G.; Terrones, H.; Xia, F.; Wang, Y. *et al.* Recent Advances in Two-Dimensional Materials beyond Graphene. *ACS Nano* **2015**, 9, 11509.

3. Das, S.; Robinson, J. A.; Dubey, M.; Terrones, H. & Terrones, M. Beyond Graphene: Progress in Novel Two-Dimensional Materials and van der Waals Solids. *Annu. Rev. Mater. Res.* **2015**, 45, 1–27.

4. Duan, X.; Wang, C.; Pan, A.; Yu, R. & Duan, X. Two-Dimensional Transition Metal Dichalcogenides as Atomically Thin Semiconductors: Opportunities and Challenges. *Chem. Soc. Rev.* **2015**, 44, 8859–8876.
5. Wang, Q. H.; Kalantar-Zadeh, K.; Kis, A.; Coleman, J. N. & Strano, M. S. Electronics and Optoelectronics of Two-Dimensional Transition Metal Dichalcogenides. *Nat. Nanotechnol.* **2012**, 7, 699–712.
6. Chhowalla, M.; Shin, H. S.; Eda, G.; Li, L. -J.; Loh, K. P. & Zhang H. The Chemistry of Two-Dimensional Layered Transition Metal Dichalcogenide Nanosheets. *Nat. Chem.* **2013**, 5, 263–275.
7. Qian, X.; Liu, J.; Fu, L. & Li, J. Quantum Spin Hall Effect in Two-Dimensional Transition Metal Dichalcogenides. *Science* **2014**, 346, 1344–1347.
8. Wilson, J. A. & Yoffe, A. D. The Transition Metal Dichalcogenides Discussion and Interpretation of the Observed Optical, Electrical and Structural Properties. *Adv. Phys.* **1969**, 18, 193–335.
9. Cho, S.; Kim, S.; Kim, J. H.; Zhao, J.; Seok, J.; Keum, D. H.; Baik, J.; Choe, D. -H.; Chang, K. J.; Suenaga, K.; Kim, S. W.; Lee, Y. H. & Yang, H. Phase Patterning for Ohmic Homojunction Contact in MoTe₂. *Science* **2015**, 349, 625.
10. Duerloo, K.-A. N.; Li, Y. & Reed, E. J. Structural Phase Transitions in Two-Dimensional Mo- and W-Dichalcogenide Monolayers. *Nat. Commun.* **2014**, 5, 1–9.

1
2
3
4
5
6
7
8
9
10
11
12
13
14
15
16
17
18
19
20
21
22
23
24
25
26
27
28
29
30
31
32
33
34
35
36
37
38
39
40
41
42
43
44
45
46
47
48
49
50
51
52
53
54
55
56
57
58
59
60

11. Kappera, R.; Voiry, D.; Yalcin, S. E.; Branch, B.; Gupta, G.; Mohite, A. D. & Chhowalla, M. Phase-Engineered Low-Resistance Contacts for Ultrathin MoS₂ Transistors. *Nat. Mater.* **2014**, 13, 1128–1134.

12. Novoselov, K. S.; Jiang, D.; Schedin, F.; Booth, T. J.; Khotkevich, V. V.; Morozov, S. V. & Geim, A. K. Two-Dimensional Atomic Crystals. *Proc. Natl Acad. Sci. USA* **2005**, 102, 10451–10453.

13. Coleman, J. N.; Lotya, M.; O'Neill, A.; Bergin, S. D.; King, P. J.; Khan, U.; Young, K.; Gaucher, A.; De, S.; Smith, R. J.; Shvets, I. V.; Arora, S. K.; Stanton, G.; Kim, H. -Y.; Lee, K.; Kim, G. T.; Duesberg, G. S.; Hallam, T.; Boland, J. J.; Wang, J. J. *et al.* Two-Dimensional Nanosheets Produced by Liquid Exfoliation of Layered Materials. *Science* **2011**, 331, 568.

14. Han, G. H.; Kybert, N. J.; Naylor, C. H.; Lee, B. S.; Ping, J.; Park, J. H.; Kang, J.; Lee, S. Y.; Lee, Y. H.; Agarwal, R. & Johnson, A. T. C. Seeded Growth of Highly Crystalline Molybdenum Disulphide Monolayers at Controlled Locations. *Nat. Commun.* **2015**, 6, 6128.

15. Naylor, C. H.; Kybert, N. J.; Schneier, C.; Xi, J.; Romero, G.; Saven, J. G.; Liu, R. & Johnson, A. T. C. Scalable Production of Molybdenum Disulfide Based Biosensors. *ACS Nano* **2016**, 10, 6173.

16. Naylor, C. H.; Parkin, W. M.; Ping, J.; Gao, Z.; Zhou, Y. R.; Kim, Y.; Streller, F.; Carpick, R. W.; Rappe, A. M.; Drndic, M.; Kikkawa, J. M. & Johnson, A. T. C. Monolayer Single-Crystal 1T'-MoTe₂ Grown by Chemical Vapor Deposition Exhibits Weak Antilocalization Effect. *Nano Lett.* **2016**, 16, 4297.

17. Kang, K.; Xie, S.; Huang, L.; Han, Y.; Huang, P. Y.; Mak, K. F.; Kim, C. -J.; Muller, D. & Park, J. High-mobility Three-Atom-Thick Semiconducting Films with Wafer-Scale Homogeneity. *Nature* **2015**, 520, 656–660.
18. Cui, X.; Lee, G. -H.; Kim, Y. D.; Arefe, G.; Huang, P. Y.; Lee, C. -H.; Chenet, D. A.; Zhang, X.; Wang, L.; Ye, F.; Pizzocchero, F.; Jessen, B. S.; Watanabe, K.; Taniguchi, T.; Muller, D. A.; Low, T.; Kim, P. & Hone J. Multi-Terminal Transport Measurements of MoS₂ Using a van der Waals Heterostructure Device Platform. *Nat. Nanotechnol.* **2015**, 10, 534–540.
19. Mak, K. F.; Lee, C.; Hone, J.; Shan, J. & Heinz, T. F. Atomically Thin MoS₂: A New Direct-Gap Semiconductor. *Phys. Rev. Lett.* **2010**, 105, 136805.
20. Lee, C.; Yan, H.; Brus, L. E.; Heinz, T. F.; Hone, J. & Ryu, S. Anomalous Lattice Vibrations of Single- and Few-Layer MoS₂. *ACS Nano* **2010**, 4, 2695–2700.
21. Danda, G; Das, P. M.; Chou, Y. -C.; Mlack, J. T.; Parkin, W. M.; Naylor, C. H.; Fujisawa, K.; Zhang, T.; Fulton, L. B.; Terrones, M; Johnson, A. T. C. & Drndic, M. Monolayer WS₂ Nanopores for DNA Translocation with Light-Adjustable Sizes. *ACS Nano* **2017**, 11, 1937–1945.
22. Kobayashi, Y.; Sasaki, S.; Mori, S.; Hibino, H.; Liu, Z.; Watanabe, K.; Taniguchi, T.; Suenaga, K.; Maniwa, Y.; Miyata, Y. Growth and Optical Properties of High-Quality Monolayer WS₂ on Graphite. *ACS Nano* **2015**, 9, 4056–4063.
23. Zhu, J.; Wu, J.; Sun, Y.; Huang, J.; Xia, Y.; Wang, H.; Wang, H.; Wang, Y.; Yi, Q. & Zou, G. Thickness-Dependent Bandgap Tunable Molybdenum Disulfide Films for Optoelectronics. *RSC Adv.* **2016**, 6, 110604–110609.

24. Lin, Y.; Dumcenco, D. O.; Huang, Y. & Suenaga, K. Atomic Mechanism of the Semiconducting-to-Metallic Phase Transition in Single-Layered MoS₂. *Nat. Nanotechnol.* **2014**, 9, 391–396.
25. Soluyanov, A. A.; Gresch, D.; Wang, Z.; Wu, Q.; Troyer, M.; Dai, X. & Bernevig, B. A. Type-II Weyl Semimetals. *Nature* **2015**, 527, 495–498.
26. Pan, X. -C.; Chen, X.; Liu, H.; Feng, Y.; Wei, Z.; Zhou, Y.; Chi, Z.; Pi, L.; Yen, F.; Song, F.; Wan, X.; Yang, Z.; Wang, B.; Wang, G. & Zhang, Y. Pressure-Driven Dome-Shaped Superconductivity and Electronic Structural Evolution in Tungsten Ditelluride. *Nat. Commun.* **2015**, 6, 7805.
27. Ali, M. N.; Xiong, J.; Flynn, S.; Gibson, Q.; Schoop, L.; Haldolaarachchige, N.; Ong, N. P.; Tao, J. & Cava, R. J. Large, Non-Saturating Magnetoresistance in WTe₂. *Nature* **2014**, 514, 205–208.
28. Naylor, C. H.; Parkin, W. M.; Gao, Z.; Kang, H.; Noyan, M.; Wexler, R. B.; Tan, L. Z.; Kim, Y.; Kehayias, C. E.; Streller, F.; Zhou, Y. R.; Carpick, R.; Luo, Z.; Park, Y. W.; Rappe, A. M.; Drndic, M.; Kikkawa, J. M. & Johnson, A. T. C. Large-Area Synthesis of High-Quality Monolayer 1T'-WTe₂ Flakes. *2D Mater.* **2017**, 4, 021008.
29. Han, G. H.; Keum, D. H.; Zhao, J.; Shin, B. G.; Song, S.; Bae, J. J.; Lee, J.; Kim, J. H.; Kim, H.; Moon, B. H. & Lee, Y. H. Absorption Dichroism of Monolayer 1T'-MoTe₂ in Visible Range. *2D Mater.* **2016**, 3, 1–6.
30. Zhou, J.; Liu, F.; Lin, J.; Huang, X.; Xia, J.; Zhang, B.; Zeng, Q.; Wang, H.; Zhu, C.; Niu, L.; Wang, X.; Fu, W.; Yu, P.; Chang, T. -R.; Hsu, C. -H.; Wu, D.; Jeng, H. -T.; Huang, Y.;

1
2
3 Lin, H.; Shen, Z. *et al.* Large-Area and High-Quality 2D Transition Metal Telluride. *Adv. Mater.*
4
5 **2017**, 29, 1603471.
6
7

8
9 31. Baroni, S.; de Gironcoli, S.; Dal Corso, A.; Giannozzi, P. Phonons and Related Crystal
10 Properties from Density-Functional Perturbation Theory. *Rev. Mod. Phys.* **2001**, 73, 515.
11
12

13
14 32. Chen, S.; Naylor, C. H.; Goldstein, T.; Johnson, A. T. C. & Yan, J. Intrinsic Phonon
15 Bands in High-Quality Monolayer T' Molybdenum Ditelluride. *ACS Nano* **2017**, 11, 814.
16
17

18
19 33. Kim, Y.; Jhon, Y. I.; Park, J.; Kim, J. H.; Lee, S.; Jhon, Y. M. Anomalous Lattice
20 Dynamics of Mono-, Bi-, and Tri-Layer WTe₂. *Nanoscale* **2016**, 8, 2309.
21
22

23
24 34. Khorasaninejad, M.; Walia, J. & Saini, S. S. Enhanced First-Order Raman Scattering
25 from Arrays of Vertical Silicon Nanowires. *Nanotechnology* **2012**, 23, 275706.
26
27

28
29 35. Kan, M.; Nam, H.; Lee, Y. H. & Sun, Q. Phase Stability and Raman Vibration of
30 Molybdenum Ditelluride (MoTe₂) Monolayer. *Phys. Chem. Chem. Phys.* **2015**, 17, 14866–
31 14871.
32
33

34
35 36. Keum, D. H.; Cho, S.; Kim, J. H.; Choe, D. -H.; Sung, H. -J.; Kan, M.; Kang, H.; Hwang,
36 J. -Y.; Kim, S. W.; Yang, H.; Chang, K. J. & Lee, Y. H. Bandgap Opening in Few-Layered
37 Monoclinic MoTe₂. *Nat. Phys.* **2015**, 11, 482–486.
38
39

40
41 37. Li, H.; Zhang, Q.; Yap, C. C. R.; Tay, B. K.; Edwin, T. H. T.; Olivier, A. & Baillargeat,
42 D. From Bulk to Monolayer MoS₂: Evolution of Raman Scattering. *Adv. Funct. Mater.* **2012**, 22,
43 1385–1390.
44
45

46
47 38. Kang, J.; Tongay, S.; Li, J. & Wu, J. Monolayer Semiconducting Transition Metal
48 Dichalcogenide Alloys: Stability and Band Bowing. *J. Appl. Phys.* **2013**, 113, 143703.
49
50
51
52
53
54
55
56
57
58
59
60

39. Zhou, S.; Han, J.; Sun, J. & Srolovitz, D. J. MoS₂ Edges and Heterophase Interfaces: Energy, Structure and Phase Engineering. *2D Mater.* **2017**, 4, 025080.
40. Berry, J.; Zhou, S.; Han, J.; Srolovitz, D. J. & Haataja, M. P. Dynamic Phase Engineering of Bendable Transition Metal Dichalcogenide Monolayers. *Nano Lett.* **2017**, 17, 2473–2481.
41. Bogaert, K.; Liu, S.; Chesin, J.; Titow, D. & Gradec, S. Diffusion-Mediated Synthesis of MoS₂/WS₂ Lateral Heterostructures. *Nano Lett.* **2016**, 16, 5129.
42. Gong, Y.; Lin, J.; Wang, X.; Shi, G.; Lei, S.; Lin, Z.; Zou, X.; Ye, G.; Vajtai, R.; Yakobson, B. I.; Terrones, H.; Terrones, M.; Tay, B. K.; Lou, J.; Pantelides, S. T.; Liu, Z.; Zhou, W. & Ajayan, P. M. Vertical and In-Plane Heterostructures from WS₂/MoS₂ Monolayers. *Nat. Mater.* **2014**, 13, 1135–1142.
43. Huang, C.; Wu, S.; Sanchez, A. M.; Peters, J. J. P.; Beanland, R.; Ross, J. S.; Rivera, P.; Yao, W.; Cobden, D. H. & Xu, X. Lateral Heterojunctions with Monolayer MoSe₂-WSe₂ Semiconductors. *Nat. Mater.* **2014**, 13, 1096–1101.
44. Ling, X.; Lee, Y. -H.; Lin, Y.; Fang, W.; Yu, L.; Dresselhaus, M. S. & Kong, J. Role of the Seeding Promoter in MoS₂ Growth by Chemical Vapor Deposition. *Nano. Lett.* **2014**, 14, 464–472.
45. Mangolini, F.; Ahlund, J.; Wabiszewski, G. E.; Adiga, V. P.; Egberts, P.; Streller, F.; Backlund, K.; Karlsson, P. G.; Wannberg, B. & Carpick, R. W. Angle-Resolved Environmental X-Ray Photoelectron Spectroscopy: A New Laboratory Setup for Photoemission Studies at Pressures up to 0.4 Torr. *Rev. Sci. Instrum.* **2012**, 83, 093112.

- 1
2
3 46. Shirley, D. A. High-Resolution X-Ray Photoemission Spectrum of the Valence Bands of
4 Gold. *Phys. Rev. B* **1972**, 5, 4709.
5
6
7
8
9 47. Moulder, J. F. & Chastain, J. Handbook of X-Ray Photoelectron Spectroscopy: A
10 Reference Book of Standard Spectra for Identification and Interpretation of XPS Data; Perkin-
11 Elmer Corporation, *Physical Electronics Division* **1992**.
12
13
14
15
16
17 48. Ueno, K. & Fukushima, K. Changes in Structure and Chemical Composition of α -MoTe₂
18 and β -MoTe₂ during Heating in Vacuum Conditions. *Appl. Phys. Express* **2015**, 8, 095201.
19
20
21
22
23 49. Laursen, A. B.; Pedersen, T.; Malacrida, P.; Seger, B.; Hansen, O.; Vesborg, P. C. &
24 Chorkendorff, I. MoS₂ —an Integrated Protective and Active Layer on n+p-Si for Solar H₂
25 Evolution. *Phys. Chem. Chem. Phys.* **2013**, 15, 20000.
26
27
28
29
30 50. Zan, R.; Ramasse, Q. M.; Jalil, R.; Georgiou, T.; Bangert, U. & Novoselov, K. S. Control
31 of Radiation Damage in MoS₂ by Graphene Encapsulation. *ACS Nano* **2013**, 7, 10167–10174.
32
33
34
35
36
37
38
39
40
41
42
43
44
45
46
47
48
49
50
51
52
53
54
55
56
57
58
59
60